

Starting vortex, separation bubbles and stall: a numerical study of laminar unsteady flow around an airfoil

By UNMEEL B. MEHTA† AND ZALMAN LAVAN

Mechanics and Mechanical and Aerospace Engineering Department,
Illinois Institute of Technology, Chicago

(Received 30 November 1973 and in revised form 28 May 1974)

The stalling characteristics of an airfoil in laminar viscous incompressible fluid are investigated. The governing equations in terms of the vorticity and stream function are solved using an implicit finite-difference scheme and point successive relaxation procedure. The development of the impulsively started flow, the initial generation of circulation, and the behaviour of the forces at large times are studied.

Following the impulsive start, the lift is at first very large and then it rapidly drops. The subsequent growth of circulation and lift is associated with the starting vortex. After incipient separation, the lift increases owing to enlargement of the separation bubble and intensification of the flow rotation in it. The extension of this bubble beyond the trailing edge causes it to rupture and brings about the stalling characteristics of the airfoil. Subsequently, new bubbles are formed near the upper surface of the airfoil and are swept away. The behaviour of the lift acting on the airfoil is explained in terms of the strength and sense of these bubbles. The lift increases when attached clockwise bubbles grow and when counterclockwise bubbles are swept away and vice versa.

1. Introduction

The theory of the flow past airfoils has attracted the attention of aerodynamicists for more than 75 years. Yet there is a lack of understanding of the phenomena associated with the stalling of airfoils. Generally, at stall laminar separation occurs followed by reattachment (usually after transition in the free shear layer); subsequently, separation may take place near the trailing edge. In addition, the striking characteristic of well-separated flows past an airfoil is their unsteadiness, which has a direct effect on the mean flow.

The steady flow past an airfoil is usually determined by boundary-layer and potential flow theories. Mathematical and physical approximations regarding the Kutta–Joukowski condition, location of the separation point, and the separated region are made; and iteration between potential flow and boundary-layer flow is required. Well-separated flows, however, cannot be handled satisfactorily

† Present address: Computational Fluid Dynamics Branch, Ames Research Center, NASA, Moffett Field, California 94035.

by this approach and solution of the Navier–Stokes equations is required. Hence, if separated regions are included, one has to iterate between potential flow, boundary-layer flow and separated flow regions that would have been continuously matched. It would be considerably more difficult to study unsteady flow by this method because each time step requires the iteration and matching procedure. The approach taken here is to eliminate this method and solve the Navier–Stokes equations numerically in the whole flow field around the airfoil. Low Reynolds number (laminar) flow is investigated to understand the physical phenomena manifested by unsteady well-separated flows and to study the relation between separation bubbles and unsteady loads. This is done by observing the time development of the flow field following the impulsive start of an airfoil. Further details of this work may be found in the doctoral dissertation of Mehta (1972).

2. Mathematical formulation

To facilitate the numerical computations, the field exterior to the airfoil is mapped into a unit circle using the transformation

$$z = \frac{1}{\kappa} + \gamma + \frac{\kappa c^2}{1 + \gamma\kappa}, \quad (1)$$

where $z = x + iy$, $\kappa = re^{i\theta}$ and $\gamma = \xi + i\eta$. A proper choice of the constants γ and c facilitates the solution for the flow over any one of the following shapes: a flat plate, a circular or elliptical cylinder and symmetric or cambered airfoils. In the present study, the trailing edge of the airfoil is rounded off by defining

$$c = [\xi + (1 - \eta^2)^{\frac{1}{2}}](1 - \delta), \quad \text{where } 0 < \delta \ll 1. \quad (1a)$$

The governing equations for the unsteady incompressible flow of a Newtonian fluid in terms of the vorticity ω and stream function Ψ are

$$H^2 r^2 \frac{R}{L} \frac{\partial \omega}{\partial t} = \left(\frac{d\rho}{dr} \right)^2 r^2 \frac{\partial^2 \omega}{\partial \rho^2} + \left(\frac{d\rho}{dr} r + \frac{d^2 \rho}{dr^2} r^2 \right) \frac{\partial \omega}{\partial \rho} + \frac{\partial^2 \omega}{\partial \theta^2} - r \frac{d\rho}{dr} \frac{R}{L} J \left(\frac{\omega, \Psi}{\rho, \theta} \right) \quad (2)$$

$$\text{and} \quad r^2 \left(\frac{d\rho}{dr} \right)^2 \frac{\partial^2 \psi}{\partial \rho^2} + \left(\frac{d\rho}{dr} r + \frac{d^2 \rho}{dr^2} r^2 \right) \frac{\partial \psi}{\partial \rho} + \frac{\partial^2 \psi}{\partial \theta^2} = -H^2 r^2 \omega, \quad (3)$$

$$\text{where} \quad H^2 = \left(\frac{\partial x}{\partial r} \frac{\partial y}{\partial \theta} - \frac{\partial x}{\partial \theta} \frac{\partial y}{\partial r} \right) / r.$$

The disturbance stream function ψ is defined as

$$\psi = \Psi - y$$

and the radial co-ordinate is stretched according to

$$\rho = (k_1 + k_2)^{-1} [\tanh^{-1}(rk_3 - k_4) + k_2], \quad (4)$$

$$\begin{aligned} \text{with} \quad k_3 &= [\tanh k_1 + \tanh k_2] [1 - r_0/(r_0 - 1)], \\ k_4 &= \tanh k_2 - r_0 [\tanh k_1 + \tanh k_2]/(r_0 - 1). \end{aligned}$$

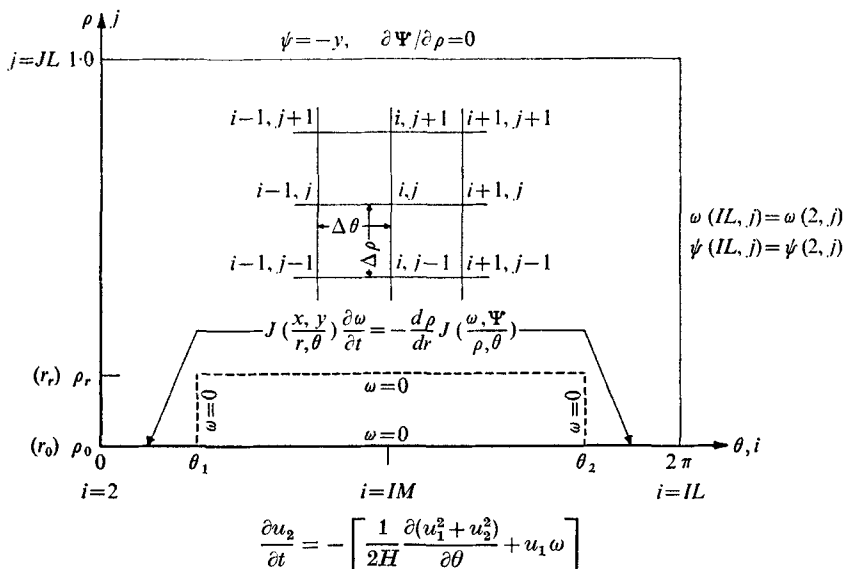


FIGURE 1. Domain of calculation, boundary conditions and grid notation.

The constants r_0 , k_1 and k_2 (all positive) determine the value of ρ . As r varies from r_0 to 1, ρ varies from 0 to 1. The Reynolds number is $R = Ul/\nu$ (l and ν are, respectively, the chord and kinematic viscosity) and L is the dimensionless chord. The stretching function (4) is introduced to obtain a better distribution of grid points in the physical plane. The grid spacing is further condensed next to the surface and is adequate away from it. The velocity components in terms of the stream function are defined as

$$u_1 = \frac{1}{rH} \left(\frac{\partial \psi}{\partial \theta} + \frac{\partial y}{\partial \theta} \right), \quad u_2 = -\frac{1}{H} \left(\frac{d\rho}{dr} \frac{\partial \psi}{\partial \rho} + \frac{\partial y}{\partial r} \right). \tag{5}$$

At Reynolds numbers much larger than unity, the vorticity directly governs the flow field near the body and the wake, and it indirectly (through the Biot–Savart law) modifies the far-field velocity and pressure. This physical phenomenon is used to break up the region of calculation into two parts: a small viscous region and a large irrotational region bounded by ρ_0 and ρ_r with $\theta_1 \leq \theta \leq \theta_2$ (figure 1). On the surface ($\rho = 1$), the constraint of no slip is applied in the form

$$\Psi = 0 \quad (\text{or} \quad \psi = -y) \tag{6}$$

and

$$\partial \Psi / \partial \rho = 0. \tag{7}$$

Condition (7) is used to calculate the surface vorticity from the stream function equation (3) with ψ replaced by Ψ . The flow at the far boundary is constrained with first-order differential relations obtained from the Navier–Stokes equations by dropping the tangential derivative of the pressure and viscous terms, i.e. at the outer boundary, the inertia terms are dominant:

$$H^2 r \frac{\partial \omega}{\partial t} = -\frac{d\rho}{dr} J \left(\frac{\omega, \Psi}{\rho, \theta} \right) \tag{8}$$

and

$$\frac{\partial \psi}{\partial \rho} = -\frac{dr}{d\rho} \left(u_2 H + \frac{\partial y}{\partial r} \right), \tag{9}$$

in which u_2 is obtained from the θ component of the Navier–Stokes equation:

$$\frac{\partial u_2}{\partial t} = - \left[\frac{1}{2rH} \frac{\partial(u_1^2 + u_2^2)}{\partial \theta} + u_1 \omega \right]. \quad (10)$$

Note that, in (10), $\omega = 0$ when $\theta_1 \leq \theta \leq \theta_2$. At $t = 0$, the flow is irrotational (without circulation), i.e. $\omega = 0$ and $\psi = -yr^2$.

These new boundary conditions are believed to be superior to specifying either potential flow or uniform velocity since ‘eddies’ or vortices can pass through the downstream boundary. Also, since the velocity far away is not defined, the circulation there can change with time. Lugt & Haussling (1972) allowed both vorticity and momentum to be transported out of the downstream boundary with the free-stream velocity when they studied the flow past an elliptical cylinder. Their use of the free-stream velocity is questionable. The convecting acceleration takes place with the local velocity not the free-stream velocity. Therefore, (8) correctly represents the vorticity transport through the downstream boundary. In (10), the absence of the tangential pressure derivative, in our opinion, will not significantly affect the motion of a vortex through the boundary.

The surface pressure distribution is obtained by integrating the tangential component of the Navier–Stokes equation:

$$p = \frac{L}{R} \frac{d\rho}{dr} \int_0^\theta \frac{\partial \omega}{\partial \rho} d\bar{\theta} \quad (11)$$

with $p(0) = 0$. The pressure coefficient C_p is therefore equal to $2p$. On the surface, the tangential stress is given by $\sigma_{12} = (L/R)\omega$. Both p and σ_{12} are made dimensionless with ρU^2 . The conventional expressions for the coefficients of lift, drag and moment around the origin of the z plane (considered positive in the counter clockwise direction) are

$$C_L = \frac{\text{lift}}{\frac{1}{2}\rho U^2 l}, \quad C_D = \frac{\text{drag}}{\frac{1}{2}\rho U^2 l}, \quad C_M = \frac{\text{moment}}{\frac{1}{2}\rho U^2 l^2},$$

with

$$\begin{aligned} C_{LP} &= -\frac{2}{L} \int_0^{2\pi} p \frac{\partial x}{\partial \theta} d\theta, & C_{LF} &= -\frac{2}{R} \int_0^{2\pi} \omega \frac{\partial y}{\partial \theta} d\theta, \\ C_{DP} &= \frac{2}{L} \int_0^{2\pi} p \frac{\partial y}{\partial \theta} d\theta, & C_{DF} &= -\frac{2}{R} \int_0^{2\pi} \omega \frac{\partial x}{\partial \theta} d\theta, \\ C_{MP} &= -\frac{2}{L^2} \int_0^{2\pi} p \left(x \frac{\partial x}{\partial \theta} + y \frac{\partial y}{\partial \theta} \right) d\theta, \\ C_{MF} &= -\frac{2}{RL} \int_0^{2\pi} \omega \left(-y \frac{\partial x}{\partial \theta} + x \frac{\partial y}{\partial \theta} \right) d\theta, \end{aligned}$$

where the subscripts P and F , respectively, represent the contributions due to pressure and viscous forces.

3. Numerical formulation

An implicit, three-point, backward, finite-difference formulation is used to solve the vorticity equation (2). The convective terms are represented by Arakawa’s (1966) second-order nine-point formula. Central differences for space

derivatives are used in the domain of calculation and at the outer boundary wherever possible. The domain bounded by $0 \leq \theta \leq 2\pi$ and $\rho_0 \leq \rho \leq 1$ is divided into a rectangular network (figure 1). The increments in θ , ρ and t are specified by $\Delta\theta$, $\Delta\rho$ and Δt with i, j and n as the corresponding indices. The finite-difference vorticity equation (2) and disturbance stream function equation (3) are written for the relaxation procedure (with the superscript k as the iteration counter) as

$$\begin{aligned}
 (\Delta\omega)_{i,j}^{n,k} = & \left\{ 2\Delta t \left\{ \omega_{i,j+1}^{n,k} \left[\left(\frac{d\rho}{dr} \right)_j^2 r_j^2 + 0.5 \left(r^2 \frac{d^2\rho}{dr^2} + r \frac{d\rho}{dr} \right)_j \Delta\rho + \frac{\Delta\rho Rr_j}{12\Delta\theta L} \left(\frac{d\rho}{dr} \right)_j \right. \right. \right. \\
 & \times \left. \left. \left(\Psi_{i-1,j+1}^{n,k} + \Psi_{i-1,j}^n - \Psi_{i+1,j+1}^{n,k} - \Psi_{i+1,j}^n \right) \right] + \omega_{i,j-1}^{n,k-1} \left[\left(\frac{d\rho}{dr} \right)_j^2 r_j^2 \right. \right. \\
 & \left. \left. - 0.5 \left(r^2 \frac{d^2\rho}{dr^2} + r \frac{d\rho}{dr} \right)_j \Delta\rho + \frac{\Delta\rho Rr_j}{12\Delta\theta L} \left(\frac{d\rho}{dr} \right)_j \left(\Psi_{i+1,j-1}^{n,k-1} + \Psi_{i+1,j}^n - \Psi_{i-1,j-1}^{n,k-1} - \Psi_{i-1,j}^n \right) \right] \right. \\
 & + \omega_{i+1,j}^n \left[\left(\frac{\Delta\rho}{\Delta\theta} \right)^2 + \frac{\Delta\rho Rr_j}{12\Delta\theta L} \left(\frac{d\rho}{dr} \right)_j \left(\Psi_{i,j+1}^{n,k} + \Psi_{i+1,j+1}^n - \Psi_{i,j-1}^{n,k-1} - \Psi_{i+1,j-1}^n \right) \right] \\
 & + \omega_{i-1,j}^n \left[\left(\frac{\Delta\rho}{\Delta\theta} \right)^2 + \frac{\Delta\rho Rr_j}{12\Delta\theta L} \left(\frac{d\rho}{dr} \right)_j \left(\Psi_{i-1,j-1}^{n,k-1} + \Psi_{i,j-1}^{n,k-1} - \Psi_{i-1,j+1}^n - \Psi_{i,j+1}^n \right) \right] \\
 & + \frac{\Delta\rho Rr_j}{12\Delta\theta L} \left(\frac{d\rho}{dr} \right)_j \left[\omega_{i+1,j-1}^{n,k-1} \left(\Psi_{i+1,j}^n - \Psi_{i,j-1}^{n,k-1} \right) + \omega_{i-1,j-1}^{n,k-1} \left(\Psi_{i,j-1}^{n,k-1} - \Psi_{i-1,j}^n \right) \right. \\
 & \left. + \omega_{i-1,j+1}^{n,k} \left(\Psi_{i-1,j}^n - \Psi_{i,j+1}^{n,k} \right) + \omega_{i+1,j+1}^{n,k} \left(\Psi_{i,j+1}^{n,k} - \Psi_{i+1,j}^n \right) \right] \Big\} \\
 & - (\Delta\rho)^2 r_j^2 RL^{-1} H_{i,j}^2 (T_2 \omega_{i,j}^{n-1} + T_3 \omega_{i,j}^{n-2}) \Big\} \\
 & \times \left\{ T_1 (\Delta\rho)^2 r_j^2 RL^{-1} H_{i,j}^2 + 4\Delta t [(\Delta\rho/\Delta\theta)^2 + (d\rho/dr)_j^2 r_j^2] \right\}^{-1} - \omega_{i,j}^{n,k-1}, \quad (12)
 \end{aligned}$$

$$\begin{aligned}
 (\Delta\psi)_{i,j}^{n,k} = & \frac{0.5}{(\Delta\rho/\Delta\theta)^2 + (d\rho/dr)_j^2 r_j^2} \left\{ \left[\left(\frac{d\rho}{dr} \right)_j^2 r_j^2 + 0.5 \left(r^2 \frac{d^2\rho}{dr^2} + r \frac{d\rho}{dr} \right)_j \Delta\rho \right] \psi_{i,j+1}^{n,k} \right. \\
 & + \left[\left(\frac{d\rho}{dr} \right)_j^2 r_j^2 - 0.5 \left(r^2 \frac{d^2\rho}{dr^2} + r \frac{d\rho}{dr} \right)_j \Delta\rho \right] \psi_{i,j-1}^{n,k-1} \\
 & \left. + (\Delta\rho/\Delta\theta)^2 (\psi_{i+1,j}^n + \psi_{i-1,j}^n) + (\Delta\rho)^2 r_j^2 H_{i,j}^2 \omega_{i,j}^{n,k} \right\} - \psi_{i,j}^{n,k-1}. \quad (13)
 \end{aligned}$$

The left-hand sides indicate the error in terms of the difference between the value of the function as determined from the finite-difference equation and its value at the previous iteration. There is no superscript denoting the iteration counter for $(i \pm 1, j)$ terms since the direction of sweep in the θ direction is altered during the iteration sequence as explained below. The three-point backward time difference is given by $T_1 = 3, T_2 = -4, T_3 = 1$ and $m = 2$; whereas the two-point backward difference is formulated with $T_1 = 2, T_2 = -2, T_3 = 0$ and $m = 1$. The latter formulation is used following the impulsive start and whenever the time step is cut in half, for the next two time steps. The truncation error for the vorticity equation (12) is $O[(\Delta\rho)^2 + (\Delta\theta)^2 + (\Delta t)^m]$; for the disturbance stream function equation (13), it is $O[(\Delta\rho)^2 + (\Delta\theta)^2]$. The above formulation of the convec-

tive terms in the vorticity equation conserves the mean vorticity and partially conserves the mean-square vorticity and mean kinetic energy (Arakawa 1970), provided that Ψ is constant along the boundary.

The no-slip condition on the surface ($j = JL$) is reformulated in terms of vorticity from the formulation of Woods (1954). The finite-difference expression with a truncation error $O[(\Delta\rho)^2]$ is

$$(\Delta\omega)_{i,JL}^{n,k} = - \left[\frac{6}{(\Delta\rho)^2} \left(\frac{d\rho}{dr} \right)_{JL}^2 \Psi_{i,JL-1}^{n,k-1} + r_{JL-1}^2 H_{i,JL-1}^2 \omega_{i,JL-1}^{n,k-1} \right] \\ \times H_{i,JL}^{-2} \left\{ 2 + 3\Delta\rho \left[\frac{dr}{d\rho} + \frac{d^2\rho}{dr^2} \left(\frac{dr}{d\rho} \right)^2 \right]_{JL} \right\}^{-1} - \omega_{i,JL}^{n,k-1}. \quad (14)$$

In the far boundary conditions (8)–(10), the θ derivative is represented by a central difference and the ρ derivative is approximated by a three-point forward difference. The time derivative is replaced as discussed before. The Jacobian in the vorticity condition (8) cannot be represented by Arakawa's formulation. The finite-difference form of this Jacobian is chosen so that its numerical value at points next to the boundary would be close to that calculated from Arakawa's formulation. This is achieved by considering the Jacobian J_K of K ($= \frac{1}{2}(u_1^2 + u_2^2)$) and Ψ for the potential flow solution around a circular cylinder. The numerical values of J_K at nodal points next to $\rho = \rho_0$ (as calculated by Arakawa's formulation) are compared with those calculated from different finite-difference forms of J_K to be used at the boundary. The following finite-difference form in terms of the vorticity residue at the outer boundary is chosen:

$$(\Delta\omega)_{i,1}^{n,k} = \{ 2\Delta t \{ (d\rho/dr)_1 (4\Delta\theta\Delta\rho)^{-1} [-4(\Psi_{i+1,2}^{n,k} - \Psi_{i-1,2}^{n,k}) \omega_{i,2}^{n,k} \\ + (\Psi_{i+1,3}^{n,k} - \Psi_{i-1,3}^{n,k}) \omega_{i,3}^{n,k} + (-3\Psi_{i+1,1}^{n,k} + 4\Psi_{i+1,2}^{n,k} - \Psi_{i+1,3}^{n,k}) \omega_{i+1,1}^{n,k} \\ - (-3\Psi_{i-1,1}^{n,k} + 4\Psi_{i-1,2}^{n,k} - \Psi_{i-1,3}^{n,k}) \omega_{i-1,1}^{n,k}] \} - (T_2 \omega_{i,j}^{n-1} + T_3 \omega_{i,j}^{n-2}) H_{i,1}^2 r_1 \} \\ \times [(T_1 H_{i,1}^2 r_1) - 6\Delta t (\Psi_{i+1,1}^{n,k} - \Psi_{i-1,1}^{n,k}) (d\rho/dr)_1 (4\Delta\rho\Delta\theta)^{-1}]^{-1} - \omega_{i,1}^{n,k-1}. \quad (15)$$

Equation (15) has a first-order truncation error in space variables; hence it contains numerical diffusion.

The disturbance stream function is obtained from the finite-difference form of (9):

$$\psi_{i,1}^{n,k} = \frac{1}{3} \left[\frac{2\Delta\rho}{(d\rho/dr)_1} \left(H u_2^{n,k} + \frac{\partial y}{\partial r} \right)_{i,1} + 4\psi_{i,2}^{n,k} - \psi_{i,3}^{n,k} \right], \quad (16)$$

where

$$(u_2)_{i,1}^{n,k} = \frac{1}{T_1} \left[-2\Delta t \left((u_1^{n,k-1} \omega^{n,k})_{i,1} + \frac{(u_1^2 + u_2^2)_{i+1,1}^{n,k-1} - (u_1^2 + u_2^2)_{i-1,1}^{n,k-1}}{4\Delta\theta(rH)_{i,1}} \right) \right. \\ \left. - (T_2 u_2^{n-1} + T_3 u_2^{n-2})_{i,1} \right] \quad (17)$$

is the finite-difference form of (10).

The present values of the vorticity and disturbance stream function at a grid point are, respectively, determined from

$$\omega^k = \omega^{k-1} + \beta_1 (\Delta\omega)^k \quad \text{and} \quad \psi^k = \psi^{k-1} + \beta_2 (\Delta\psi)^k,$$

where β_1 and β_2 are relaxation parameters. For the k th iteration at any time t , the values of ω and ψ are determined at each nodal point by sweeping in the

general direction of the free stream, i.e. from $\theta = \pi$ to 0 and from $\theta = \pi$ to 2π so that the numerical errors are propagated downstream, and away from the surface from $\rho = 1$ to ρ_0 since the surface is the source of vorticity. Furthermore, when k (the iteration number) is odd, the direction of calculation is from $\theta = \pi$ to 2π followed by $\theta = \pi$ to 0, whereas this order is interchanged for k even.

Computations of pressure coefficients on the surface and loads are conducted for each time t with a finite-difference integration formula derived by combining two four-point expressions (in order to have a lower effective truncation error). The integral of a function $f(\rho, \theta)$ between the nodal points i and $i + 1$ on the surface is expressed as

$$I = \frac{1}{30}(11I_1 + 19I_2),$$

where

$$I_1 = \frac{1}{24}\Delta\theta (9f_i + 19f_{i+1} - 5f_{i+2} + f_{i+3}),$$

$$I_2 = \frac{1}{24}\Delta\theta (-f_{i-1} + 13f_i + 13f_{i+1} - f_{i+2}).$$

This formula is used first to determine the pressure from (11) and then the loads. The pressure calculations require the normal vorticity gradient, which is represented as

$$\partial\omega/\partial\rho = (\omega_{JL} - \omega_{JL-1})/\Delta\rho.$$

This equation has a truncation error $O(\Delta\rho)$. A formula with a smaller truncation error is not used because the derivation of the surface vorticity with a truncation error $O(\Delta\rho^2)$ requires the use of a formula identical to the above equation for $\partial(H^2r^2\omega)/\partial\rho$.

4. Computation data, accuracy and computer plots

The computations are conducted for an airfoil at 15° incidence with $R = 1000$. The shape of the airfoil is defined by $\xi = -0.05214$, $\eta = 0$ and $\delta = 0.025$ in (1a). It has an 8.9998% thick symmetric profile with maximum thickness at 28.89% chord. In transformation (4), $k_1 = 2.0$ and $k_2 = 2.8$. The grid distribution and subdivision of the domain into rotational and irrotational parts are determined from $IL = 82$, $JL = 48$, $r_0 = 0.02$ ($\rho_0 = 0$), $\rho_r = 0.31915$ ($r_r = 0.089796$), $\theta_1 = 0.8639$ rad and $\theta_2 = 4.791$ rad. The values of ρ_r and ρ_0 , respectively, correspond to (approximately) $x = 3.0$ chords and $x = 13.4$ chords. The total number of node points used is 3840, with 3024 points in the rotational region and 816 in the irrotational domain. The resulting grid distribution in the vicinity of the airfoil is shown in figure 2. The first node point downstream of the trailing edge is at a distance of 5.567×10^{-5} chord. In the relaxation procedure, $\beta_1 = 0.09$ and $\beta_2 = 1.9$ are used at all time steps.

Table 1 gives the different time steps used during the calculations. The distances travelled by the airfoil during $\Delta t = 0.001$ and 0.512 correspond, respectively, to 0.000269 and 0.1379 chord. The time step Δt is altered to yield changes in C_p on the surface that are neither small nor severe. Table 1 also shows the average values of both the number of iterations (required for a satisfactory result) and the maximum (magnitude) residues of the disturbance stream function and vorticity (when the iteration procedure is stopped) during each time

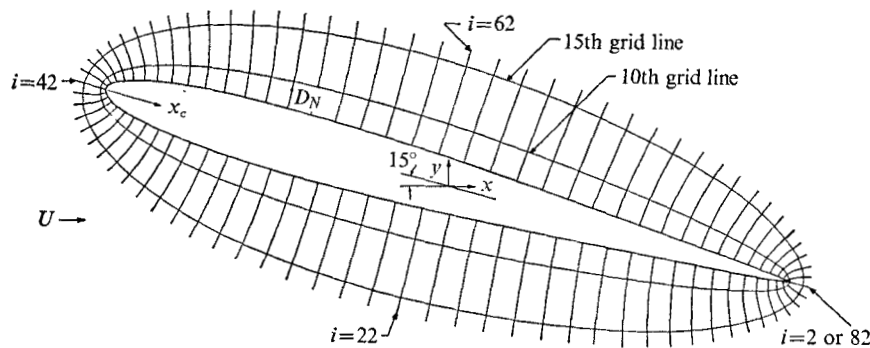


FIGURE 2. Grid distribution around 9% thick symmetric airfoil at $\alpha = 15^\circ$.

Number	t_1-t_2	Δt	Number of Δt steps	k_{\max} (aver- age)	$\Delta\psi$ (average)	$\Delta\omega$ (average)	ΔC_p (%) (average)
1	0.000-0.006	0.001	6	147	2.43×10^{-6}	0.298	1.468
2	0.006-0.012	0.002	3	200	1.09×10^{-5}	0.212	1.593
3	0.012-0.020	0.004	2	200	6.30×10^{-7}	0.130	1.082
4	0.020-0.036	0.008	2	200	1.51×10^{-6}	4.007	4.258
5	0.036-0.116	0.016	5	200	3.73×10^{-6}	2.199	3.605
6	0.116-0.276	0.032	5	340	3.91×10^{-6}	0.647	2.928
7	0.276-0.596	0.064	5	420	5.16×10^{-6}	0.295	1.446
8	0.596-1.620	0.128	8	400	1.07×10^{-5}	0.713	6.735
9	1.620-3.668	0.256	8	461	1.35×10^{-5}	0.448	2.936
10	3.668-11.348	0.512	15	553	8.40×10^{-6}	0.330	1.460
11	11.348-13.140	0.256	7	499	1.92×10^{-6}	0.425	2.857
12	13.140-19.540	0.128	50	638	1.81×10^{-6}	0.458	3.216
13	19.540-28.756	0.256	36	795	1.19×10^{-6}	0.456	3.168
Total or average			152	568	3.83×10^{-6}	0.546	3.015

TABLE 1. Summary of time increments, number of iterations, residues and errors

interval. The last row in the table gives the average values of the 152 time increments. With single-precision calculations on a UNIVAC 1108 (a 36-bit machine), it was not possible to achieve, in general, values of the vorticity residue less than $O(10^{-1})$. However, this residue relative to the value of the vorticity at the trailing edge is $O(10^{-4})$ following the impulsive start; the residue is $O(10^{-2})$ – $O(10^{-1})$ when the maximum vorticity in the field is $O(10^{+2})$.

The values of the pressure are calculated by integrating (11) from $\theta = 0$ to π and again from 2π to π . The average of the two values thus determined at $\theta = \pi$ is reported and used in subsequent calculations of loads. Furthermore, these calculations are repeated by reversing the integration directions, i.e. from the leading to the trailing edge along both surfaces. The latter procedure gives better values on the whole, probably since the radius of curvature at the leading edge is much larger than at the trailing edge. The last column in table 1 reports the average percentage errors for selected C_p values.

t	0.084	0.276	0.596	0.980	1.620
x_{cl}	0.012628	0.012628	0.012628	0.012628	0.012628
C_p	1.434	1.240	1.168	1.135	1.107
t	6.228	8.788	19.156	23.124	28.500
x_{cl}	0.022387	0.022387	0.0056235	0.012628	0.012628
C_p	1.084	1.085	1.055	1.063	1.050

TABLE 2. Variation of C_p near front stagnation point with time

Table 2 gives the variation of the true pressure coefficient near the front stagnation point with time. In this case, the r -momentum equation is integrated from upstream along the first θ line located upstream of the front stagnation point. In the table, x_c denotes the normalized distance (with respect to the chord) measured from the leading towards the trailing edge along the chord of the airfoil (figure 2). Subscripts l and u represent the lower and upper surfaces of the airfoil, respectively. After the influence of the impulsive start is no longer felt next to the surface (say after $t = 6.228$), the value of C_p remains near unity. Note that the quasi-steady Bernoulli equation gives the value of unity for the stagnation-point pressure coefficient (once the initial transient period is over). The calculated value is larger than unity because the Reynolds number of the flow is not large enough, and it does not remain constant because of the unsteady nature of the flow.

Streamlines and equi-vorticity lines are mapped using an incremental plotter. The numerical values of the stream function for the plotted streamlines vary from -0.40 to 0.32 with an increment of 0.04 ; the vorticity values for the plotted equi-vorticity lines vary from -9.0 to 7.0 with an increment of 2.0 . (An animated movie showing the flow development in terms of instantaneous streamlines and equi-vorticity lines is available on loan from the authors.)

5. Flow field after impulsive start

In a very short time, the rear stagnation point moves from its location for potential flow to the neighbourhood of the trailing edge and the front stagnation point moves up the airfoil (figures 3*a* and 4*a*). As suggested by Batchelor (1967, pp. 438–441) this movement of the rear stagnation point is accompanied by a counterclockwise separation bubble (defined as the region bounded by an instantaneous zero streamline) between the rear stagnation point and the trailing edge. The rear dividing streamline leaves the airfoil practically at the trailing edge when $t > 0.006$. This suggests that immediately after an impulsive start the circulation is zero. Thereafter, the front stagnation point reverses its direction of motion and moves downstream, while the rear stagnation point remains practically at the trailing edge.

Figures 3 and 5(*a*) show that the positive equi-vorticity lines situated along the lower surface curl up near the trailing edge. A comparison of the streamlines and the equi-vorticity lines near the trailing edge indicates a wavy pattern (or

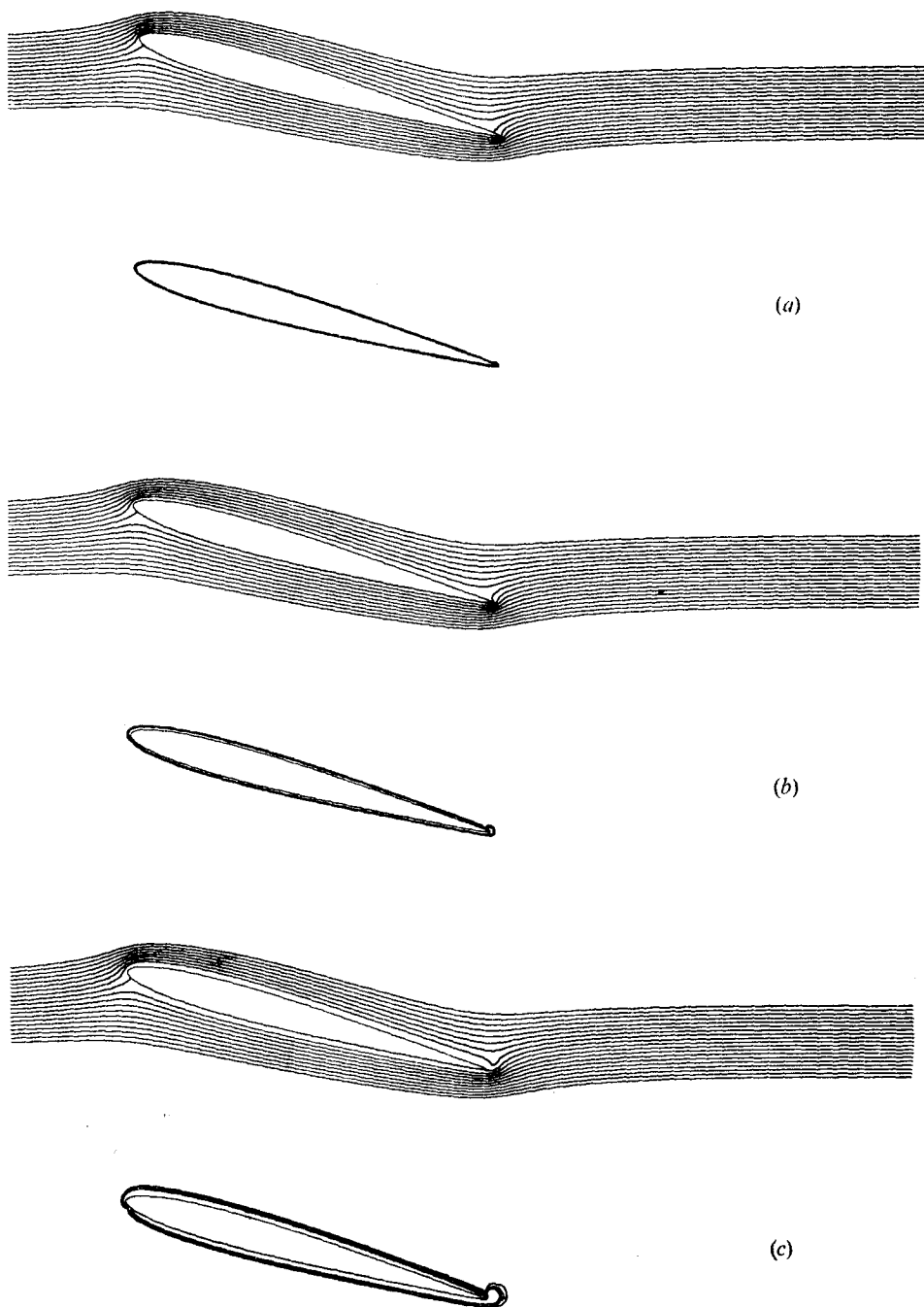


FIGURE 3. Streamlines and equi-vorticity lines. (a) $t = 0.001$. (b) $t = 0.016$.
(c) $t = 0.148$.

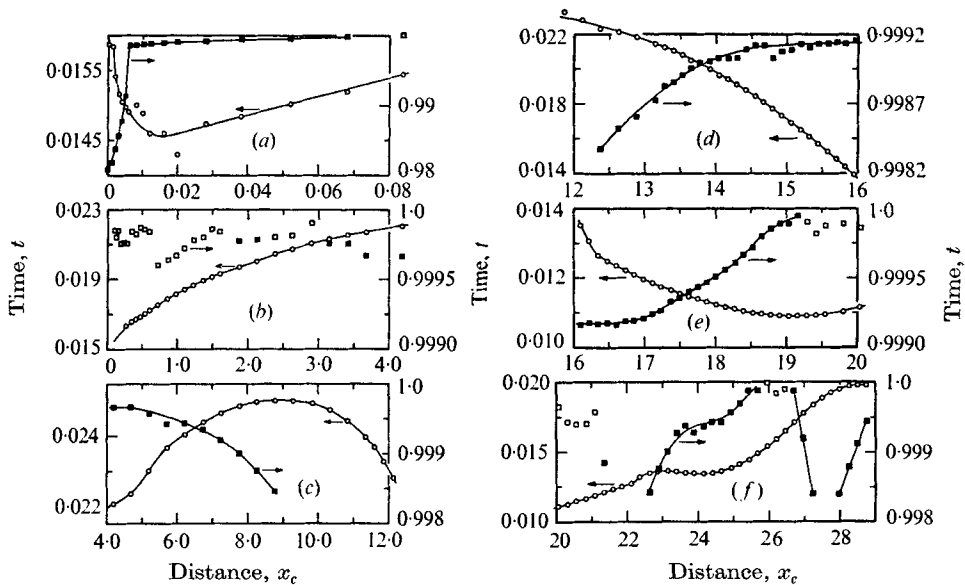


FIGURE 4. Locations x_c of front (circles) and rear (squares) stagnation points. Open symbols, lower surface; solid symbols, upper surface.

valleys) along streamlines which corresponds to the concentric equi-vorticity lines of the starting vortex. There is a remarkable qualitative similarity between these instantaneous streamlines and the photographs of Prandtl & Tietjens (1934, pp. 296–299). The equi-vorticity plots in figure 3 clearly show that diffusion dominates following the impulsive start. As time increases, the effect of convection is first felt downstream of the trailing and the leading edges along the upper surface.

The asymmetry of the flow field at $t = 0^+$ gives rise to a similar skew surface vorticity, shown for $t = 0.003$ in figure 6(a). At small times, the pressure coefficient C_p is large and it decreases with time as shown in figure 7. Since the normal vorticity gradients at the surface are proportional to the tangential pressure gradients, they follow the same trend. An adverse pressure gradient near the leading edge (on the upper surface) at $t = 0.02$ indicates the presence of vorticity sources due to convection of vorticity from upstream. This results in a local vorticity minimum. The value of C_p at the front stagnation point decreases with time (figure 8a) and the region over which there is an adverse pressure gradient extends in length along the upper surface.

The vorticity profile and the flow directions normal to the surface at the leading edge are shown in figure 9. The normal distance D_N is measured in the z plane (figure 2) from the surface in the direction that corresponds to a line of constant θ in the transformed plane. The velocity increases rapidly to a large value within a short normal distance where vorticity is still large (figure 10) and then it decreases. Note that the first-order boundary-layer and potential flow theory does not give maximum velocity within the boundary layer. As time advances, this maximum value falls because the fluid is retarded (or the apparent thickness of the airfoil is increased). The angle β , which shows the direction of flow

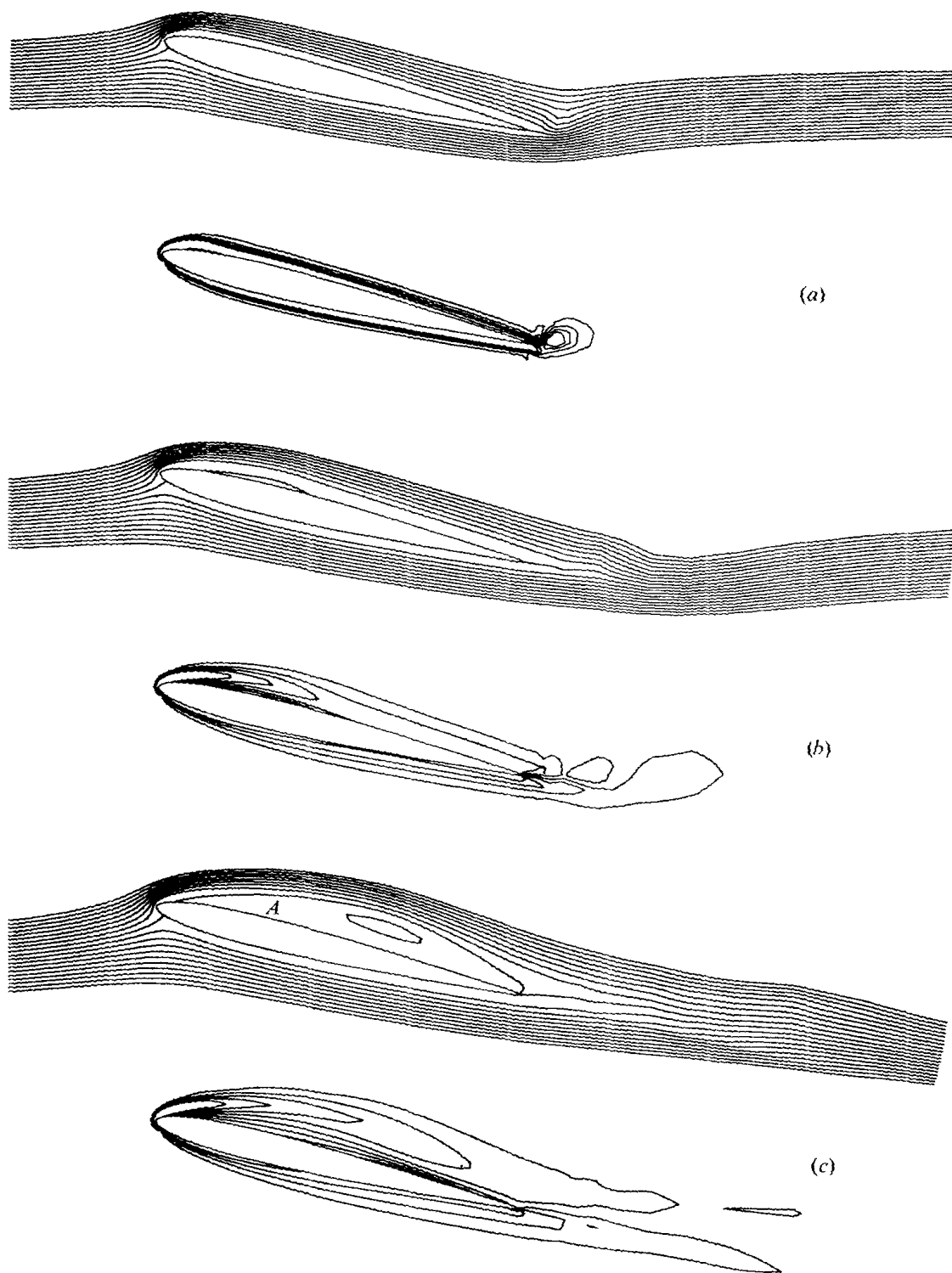


FIGURE 5. Streamlines and equi-vorticity lines. (a) $t = 0.596$.
 (b) $t = 2.388$. (c) $t = 7.252$.

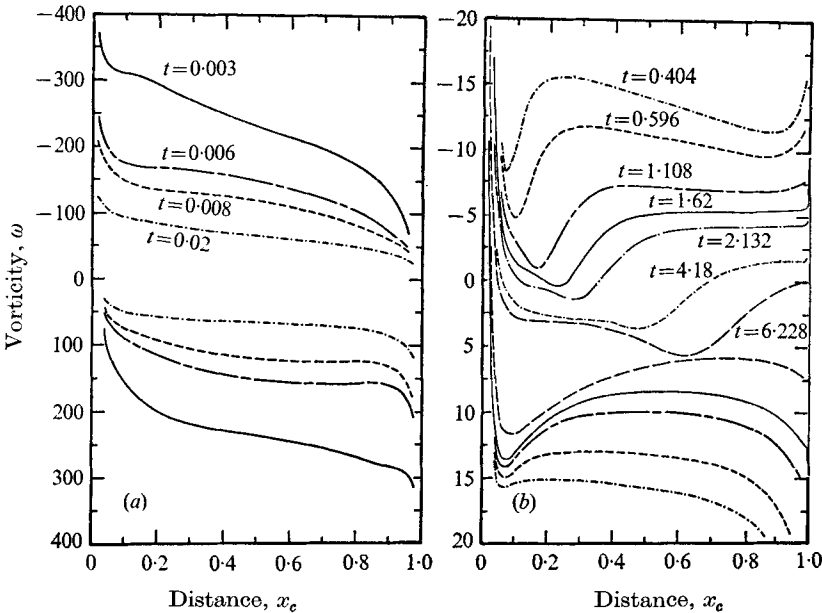


FIGURE 6. Surface vorticity distributions. $t = 0.003\text{--}6.228$.

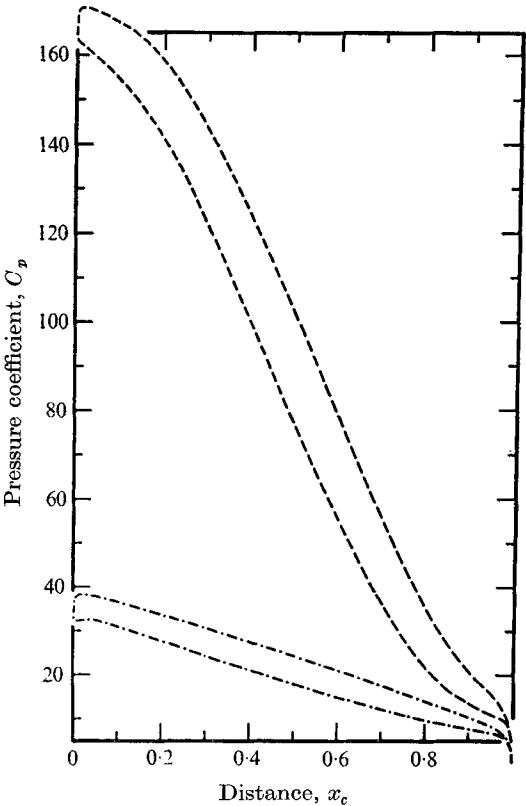


FIGURE 7. Surface pressure coefficients. ---, $t = 0.008$; — · —, $t = 0.020$.

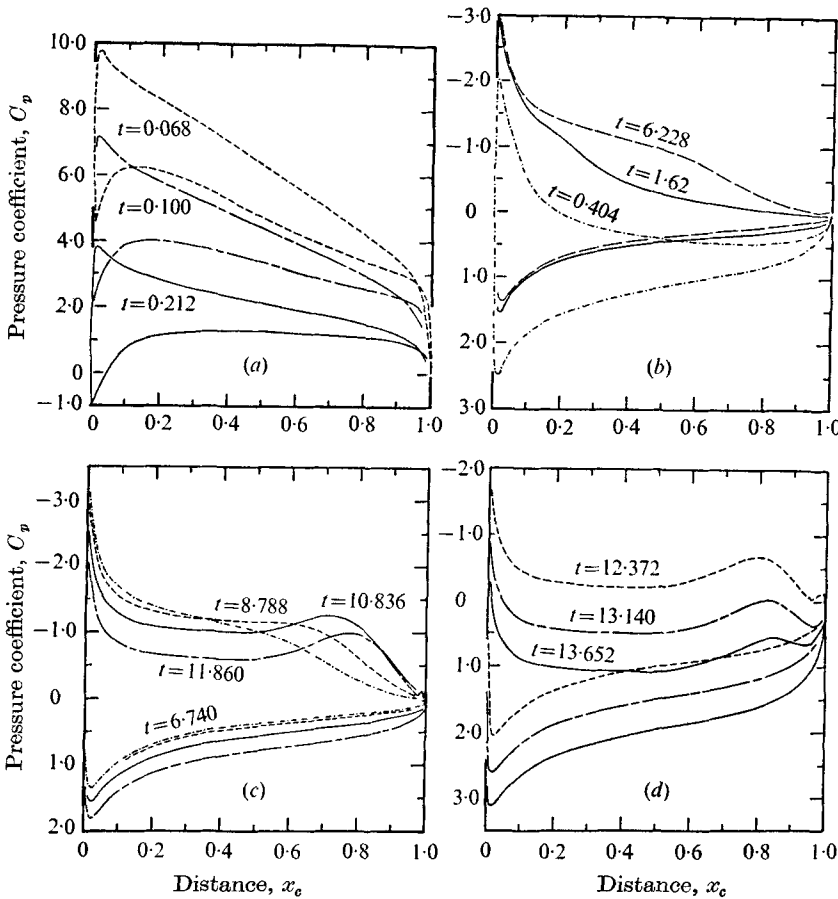


FIGURE 8. Surface pressure coefficients. $t = 0.068\text{--}13.652$.

measured from the positive- x axis in the counterclockwise direction, also increases (figure 9*b*) as the main flow is displaced outwards. The magnitude of the potential flow velocity at $t = 0^+$ is 2.2655 at the leading edge, whereas its value with circulation (that makes the velocity zero at the trailing edge) is 4.53126. (The Kutta–Joukowski condition is not applicable since the airfoil does not have a sharp trailing edge.) When $t = 0.002$, the magnitude of the maximum velocity is 1.8283 at $D_N = 0.007881$. At the trailing edge, initially, the vorticity and the velocities are higher than at the leading edge because of the larger curvature.

Taneda (1972) investigated experimentally the development of lift for an impulsively started elliptical cylinder at incidence. He reports that at the beginning of the motion a marked peak in the lift occurs. This peak nearly vanishes within a short time, then the lift increases again. This agrees with figures 11(*a*) and (*b*), which show that there is a high value of C_L right after the impulsive start which diminishes up to $t = 0.596$ and then again increases. The equi-vorticity lines (figures 3 and 5*a*) show more positive vorticity than negative downstream of the trailing edge. The net vorticity (positive) is enhanced and moves down-

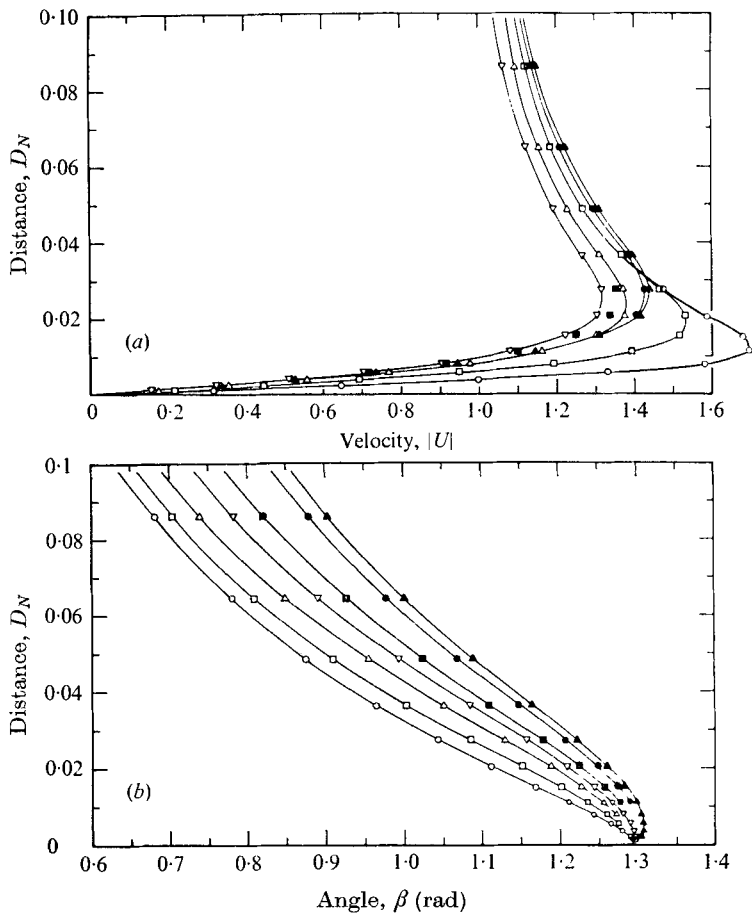


FIGURE 9. Velocity and flow-direction profiles at $x_c = 0$.

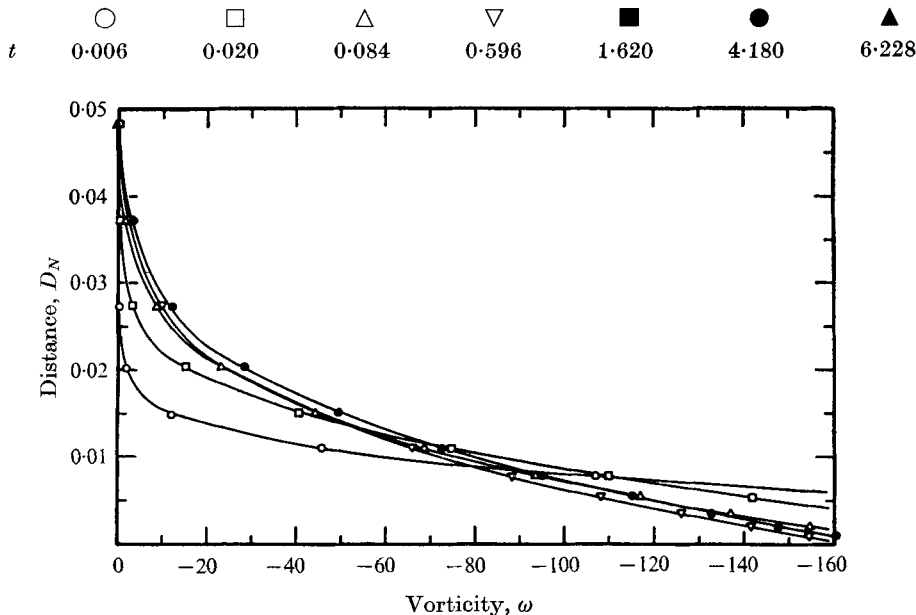


FIGURE 10. Vorticity profiles at $x_c = 0$. Symbols as in figure 9.

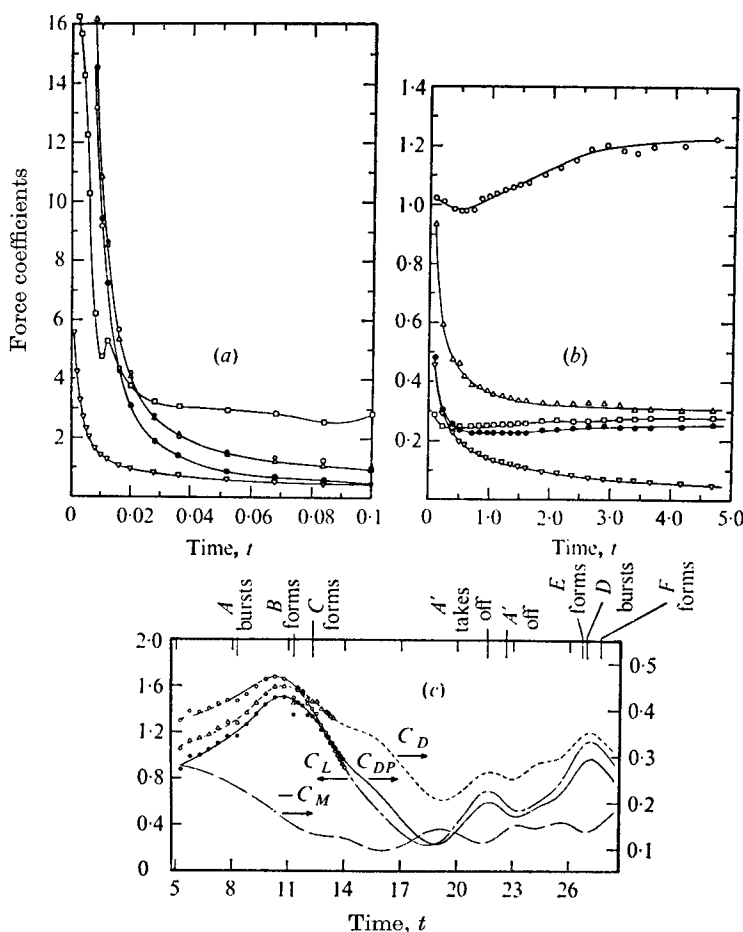
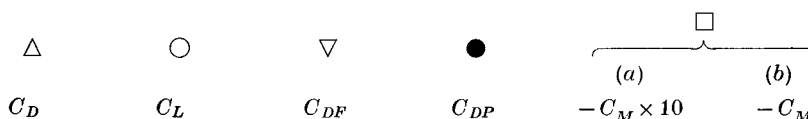


FIGURE 11. Time histories of loads.



stream as time increases. This brings about a change in the velocity field in the sense that a circulating motion is superimposed on the translatory motion of the fluid. The major contribution of the starting vortex in terms of circulation and lift is felt after the front stagnation point starts moving down the airfoil. The augmentation of the circulation is also suggested by the downward motion of the dividing streamline both upstream and downstream of the airfoil. Hence the classical relationship between lift and circulation does not hold at small t . The initial high values of the lift are a direct consequence of the impulsive start, whose influence at the beginning decays at an extremely rapid rate next to the surface.

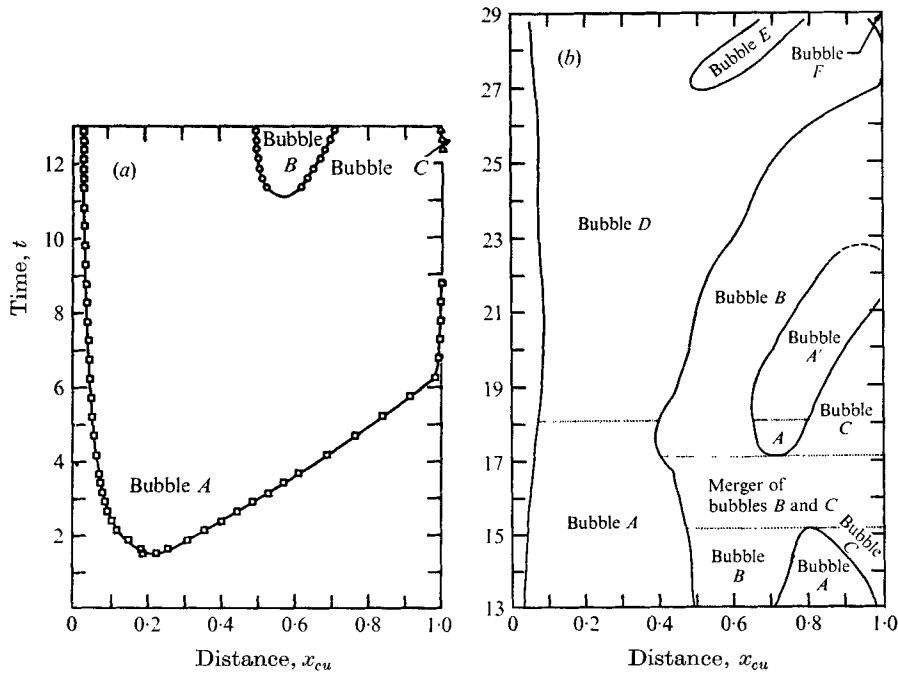


FIGURE 12. Locations of vanishing vorticity on the upper surface of the airfoil.

6. Growth of separation bubble and lift coefficient

In this section, the onset of separation and the growth of the separation bubble are explained. The increase in the lift coefficient after separation is related to the growth of this bubble in terms of its size and strength. Before discussing these results, a few comments regarding separation bubbles, vortices and separation points are necessary.

A bubble is said to be open (or burst) if it is not completely enclosed by a zero streamline and there is a closed streamline loop within this region. A vortex is defined by closed equi-vorticity lines. Bubbles and vortices are separate entities that may have some region in common. The attached bubble is bounded by a streamline with a stream function value of zero. This is brought about at any instant by a bifurcation of the surface streamline and the recombination of the branches. For a ruptured bubble, there is a completely 'separated' instantaneous streamline. The bifurcation point is called here the separation point and the unification point is named the reattachment point of the bubble.

Sears & Telionis (1971) proposed a criterion for unsteady separation based on the appearance of a Goldstein (1948) singularity, which is a peculiarity of the boundary-layer equation. Our definition of a separation point, as a location at which the instantaneous streamline bifurcates and downstream of which there is reverse flow, is based on the physical behaviour of the flow. Brown & Stewartson (1969), after repeated careful experiments and observations, report that in two-dimensional (steady) flow the main stream breaks away at or very near the point

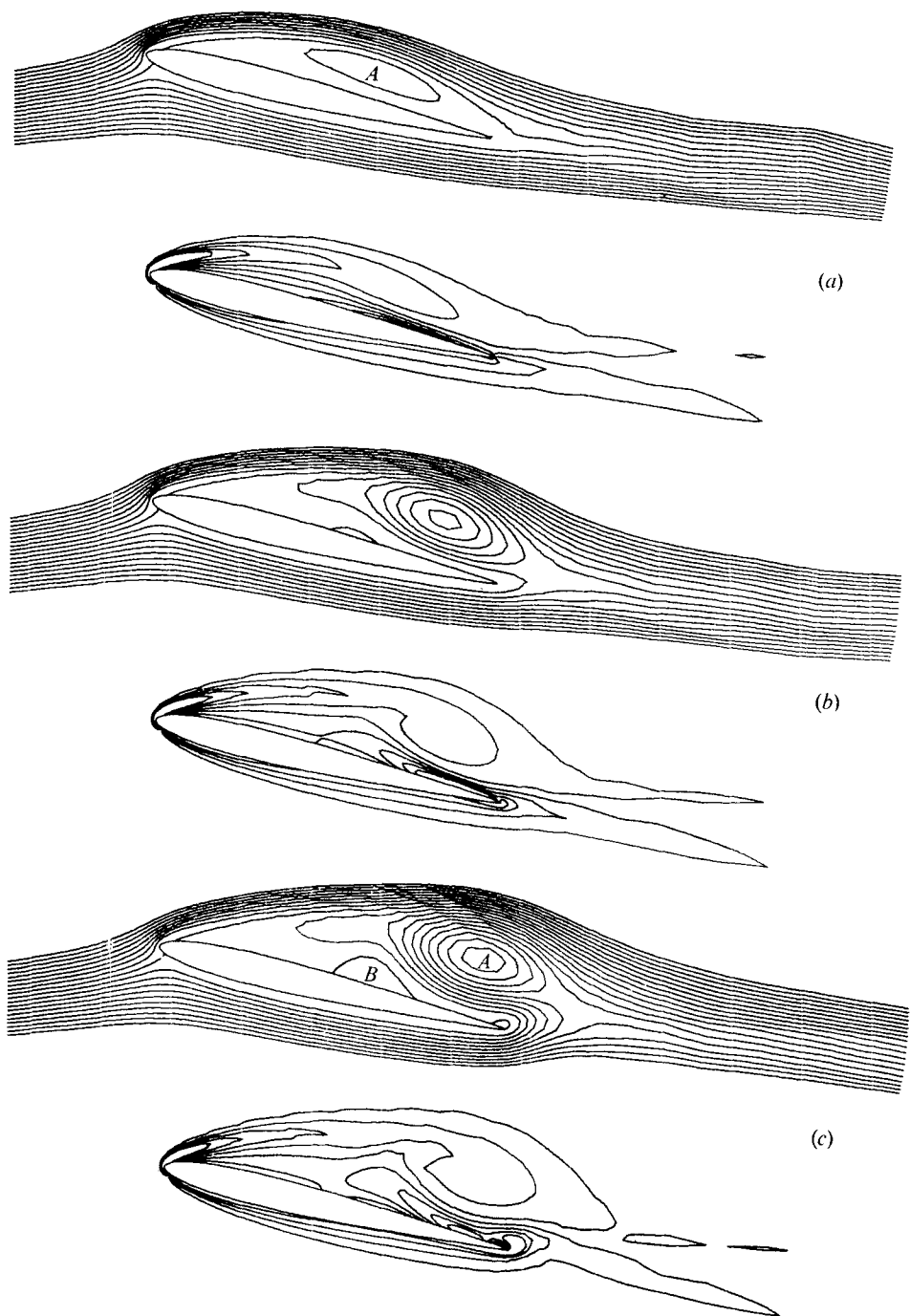


FIGURE 13. Streamlines and equi-vorticity lines. (a) $t = 8.276$.
(b) $t = 11.860$. (c) $t = 13.780$.

where the skin friction on a stationary body vanishes. In the present study, the streamline bifurcation point is very near (or at) the location where the vorticity (or skin friction) is zero.

When a circular cylinder is started impulsively from rest, the flow separates first at the rear stagnation point. In the present study, a point of vanishing shear first appears near the leading edge (at $x_{cu} = 0.205$, figure 12*a*), instead of at the trailing edge. This point is a coalescence of a separation point and a reattachment point. The strength of separation bubble A increases with time, as indicated for example by the presence of the $\Psi = -0.04$ streamline (inside the bubble) in figure 5(*c*). The width of the bubble also extends with time, and the streamlines widen over the rear of the bubble. Figure 13(*a*) shows an open bubble at the downstream end. Bubble A bursts just off the surface. Consequently, there is a small bubble between the reattachment point and the rear stagnation point (note the black dot at the trailing edge in figure 13*a*). The stagnation point becomes the separation point of the new bubble and the reattachment point of bubble A becomes the reattachment point of this bubble. The size of the bubble decreases and the separation and reattachment point combine to dissolve it.

The downstream motion of the starting vortex and the diffusion of its vorticity are shown in figures 5(*a*) and (*b*). The structure of this vortex is not preserved as time advances. The convective effect near the leading edge at $t = 0.596$ (figure 5*a*) is shown by the presence of two $\omega = -9.0$ lines. This effect is even more pronounced in figure 5(*b*), where equi-vorticity lines for $\omega = -5$, -7.0 and -9.0 have turned around towards the leading edge. Both positive and negative equi-vorticity lines exist along the upper surface when there is a separation bubble (figure 13*a*). Consequently, the zero-vorticity line passes through this bubble, which is unlike either a starting vortex or a solid-body rotation.

Stuart (1971), while discussing the flow field around a circular cylinder started impulsively from rest, states that after a short time a separation bubble is produced at the rear of the cylinder “but still within the boundary layer”. He hesitates to label this phenomenon as separation since it does not involve a large-scale breakaway of fluid. Sears & Telionis (1971) maintain that the definition of unsteady separation must be based on physical phenomena such as the shedding of vorticity into the flow, but not flow reversal in general. They further state that when the vorticity of the boundary layer, or at least its outer part, is carried out into the flow (shedding of vorticity), the flow ceases to be of boundary-layer character. Finally, Wang (1971) holds the view that the definition of unsteady separation from physical phenomena, such as the shedding of vorticity and actual flow reversal (on a fixed body), cannot be formulated by any of the existing theories. He concludes that only a Lagrangian description of pathlines can characterize such unsteady phenomena.

In the light of these comments, it is constructive to compare the equi-vorticity lines. Below the airfoil, from the front stagnation point to the trailing edge there is a boundary-layer-type flow at all times. Similarly, along the upper surface, there are smooth equi-vorticity lines spanning the length of the airfoil at small times (figures 3 and 5*a*). While bubble A is growing, vorticity is being convected laterally away from the surface (figures 5*b* and 13*a*). Immediately after bubble A

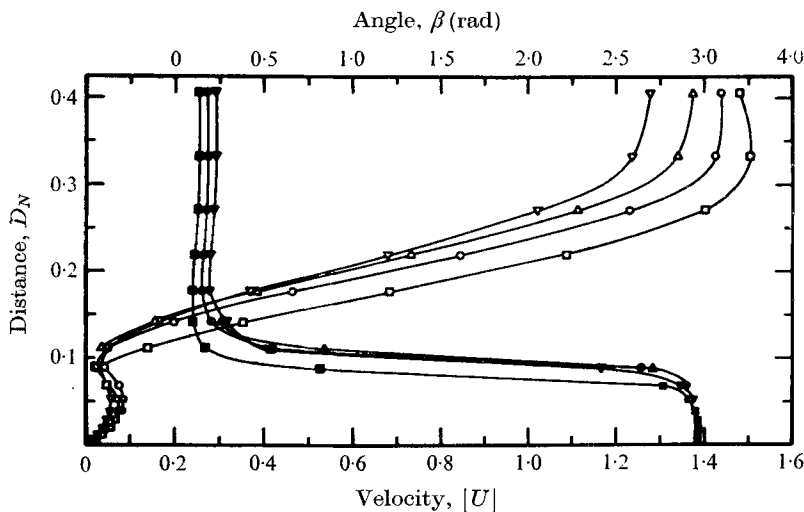


FIGURE 14. Velocity and flow-direction profiles at $x_{cu} = 0.1353$.

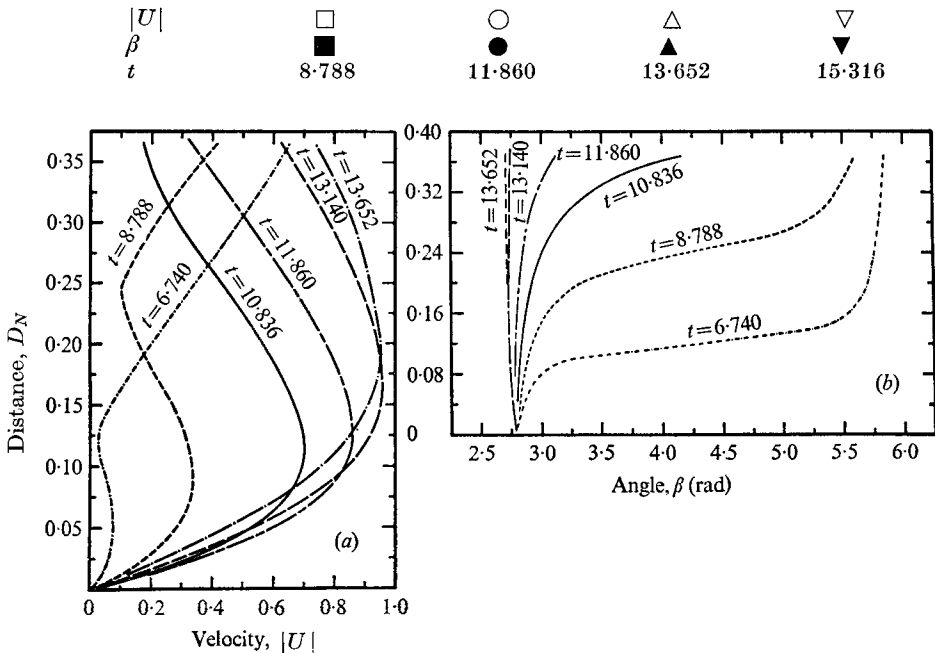


FIGURE 15. Velocity and flow-direction profiles at $x_{cu} = 0.8406$.

bursts, the basic pattern of the equi-vorticity lines does not change. Hence a distinction between a local separation bubble as part of a boundary layer and a large-scale breakaway of fluid is not available from these figures.

The surface vorticity and the pressure distributions are given, respectively, in figures 6(b) and 8(b) and (c). At all times, there are sharp variations in vorticity near the trailing edge as shown, for example, for $t = 1.620$. The variation in vorticity suggests that separation occurs downstream of the location at which the magnitude of the vorticity is minimum (or where the gradient of vorticity

along the surface is zero). Until bubble *A* bursts, the lower surface is under the influence of the impulsive start. The bump near $x_{cu} = 0.2$ in the pressure distribution at $t = 1.620$ (figure 8*b*) reveals the presence of the separation bubble. The growth and downstream movement of this bubble are accompanied by a small drop in the suction peak (relative to C_p at the front stagnation point), and a practically uniform pressure develops along the first half of the bubble figure 8*c*, $t = 10.836$).

Bubble *A* alters the pressure distribution on the surface and thereby lowers the leading-edge suction peak. Downstream of the maximum bubble height, there is a region of pressure recovery. While the bubble is extending over the airfoil, the pressure at the point of reattachment is greater than at separation, although not so great as that for the hypothetical flow in its absence. (Hence the bubble could be regarded as a 'device' adopted by the fluid to diminish the positive pressure gradients on the surface.) When it extends into the wake, the pressure at the trailing edge is reduced. Across the bubble, the normal distance from the surface at which the vorticity becomes zero is shorter than the distance at which the velocity becomes minimum. This minimum velocity is different from zero and is associated with a drastic change in the direction of the flow (e.g. see figure 14 for $x_{cu} = 0.1353$). The magnitude of the reverse flow (during the time interval $t = 1.450$ – 10.836) is less than 0.1 at $x_{cu} = 0.1353$ and at $x_{cu} = 0.4760$ it is less than 0.26. However, at $x_{cu} = 0.8406$ when $t = 10.836$, it is as large as 0.697 and is increasing (figure 15).

The loads acting on the airfoil between $t = 0.596$ and 10.836 are shown in figures 11(*b*) and (*c*). The value of C_L increases during this time interval; maximum lift is attained when the bubble extends beyond the trailing edge while C_{DF} continues to diminish up to $t = 9.812$. This drop is explained by the facts that, along the surface in contact with the separation bubble, the friction force does not act as drag and, on the lower surface, the vorticity continues to decrease until after the rear stagnation point moves into the flow field. C_{DP} drops from its high initial values until incipient separation and then it rises since the effective thickness (as judged by the shape of the outer instantaneous streamline) of the airfoil is increased by the bubble. The net result of the friction and pressure drag is to reduce the total drag up to $t = 4.180$ and then to raise it. The value of C_L is approximately three to four times C_D . The value of C_M increases up to $t = 4.180$ and then decreases. The inviscid C_L for the present investigation, which includes (Thwaites 1960, p. 194) the influence of the thickness of the airfoil, is 1.775. (It is the circulation around the airfoil that makes the trailing edge a stagnation point.) However, for the NACA 0009 airfoil at the same angle of attack and with $R = 6 \times 10^6$, experiments indicate that $C_L = 1.25$, $C_D = 0.0127$ and $C_M = -0.15$ (Abbott & Von Doenhoff 1959, pp. 454–455). In the present study, the value of C_D is an order of magnitude larger than the above value; $C_L = 1.68$ when $t = 10.324$.

During the time interval under consideration, C_L increases as the size and strength of bubble *A* increase because (i) the effective thickness of the airfoil becomes larger, (ii) the bubble is able to sustain lower surface pressures, (iii) the net negative vorticity, which induces clockwise circulation, rises above the upper

surface (compare the location of the $\omega = -1.0$ vorticity line in figures 5*a* and 13*a*), (iv) the front stagnation point moves down the lower surface up to $t = 8.788$ (figures 4*b* and *c*), and (v) the dividing streamline ($\Psi = 0$) moves downwards both upstream and downstream of the airfoil.

7. Anatomy of the flow around a stalled airfoil

Two new counterclockwise bubbles develop on the surface and, consequently, the lift decreases. When these bubbles are cast off, C_L increases and, eventually, one clockwise bubble remains. This sequence, which began when bubble *A* burst, is discussed below. Finally, a comparison with other studies is made.

A new bubble appears in figure 13(*b*), near $x_{cu} = 0.55$. (This bubble is labelled *B*.) The direction of flow in this bubble is counterclockwise, opposite to that in bubble *A*. Bubble *B* develops because of the adverse pressure gradient for the upstream flow next to the surface in bubble *A*. The strength of bubble *A* grows with time and bubble *B* expands (figures 13*b* and *c*). Also, the centre of bubble *A* moves downstream. A new counterclockwise bubble (*C*) appears at $t = 12.372$ near the trailing edge. Bubble *B* primarily grows along the downstream direction whereas bubble *C* mainly extends up the chord. They coalesce (figure 12*b*) and increase in size and strength, while preserving two separate centres (figure 16*a*); later, both bubbles *B* and *C* regain their separate identities. At $t = 17.236$ (figure 16*b*), the maximum distance in the y direction between $\omega = 1.0$ and -1.0 is nearly twice the projected length of the airfoil. The movement of the front stagnation point up the airfoil (figures 4*c-e*) indicates that the circulation around the airfoil diminishes. The overall trend of the dividing streamline is to shift upwards.

The downstream motion of the centre of ruptured bubble *A* causes stall, precipitating a sequence of events: (i) negative pressure gradients upstream of the location of maximum bubble height develop on the surface; (ii) the formation of counterclockwise bubble *B* decreases the positive pressure gradients created by bubble *A* near the trailing edge; (iii) negative pressure gradients (figure 8*d*) near the trailing edge, with the flow moving upstream, form the counterclockwise bubble *C*, which augments these negative pressure gradients; (iv) the bubbles coalesce and (v) separate again. Overlaying this sequence on the time history of the loads (figure 11*c*), we observe that (*a*) the growth of C_L diminishes when event (i) begins; (*b*) C_L falls just before bubble *B* is formed; (*c*) events (iii) and (iv) lower C_L further; (*d*) the rate of decrease in C_L is less when event (v) starts. C_D behaves in the same manner. However, the moment coefficient is out of phase: it peaks before both C_L and C_D .

Bubble *B* splits bubble *A* and opens to the outside flow as observed in figure 16(*c*). (The bubble near the leading edge is labelled *D* and the second part of the original bubble *A* is called *A'*.) Bubbles *D* and *A'*, as shown here or in figure 17(*a*), compare remarkably well with those photographed by Prandtl (1952, figure 3.83, p. 200) over a stalled airfoil (see also Batchelor 1967, figure 5.11.1(*b*), plate 7). The strength of bubble *C* intensifies, it moves downstream and it lifts off the airfoil. The reattachment point of bubble *D* and the separation point of bubble *A'* move down the airfoil (figure 12*b*). Later, bubble *A'* also disengages

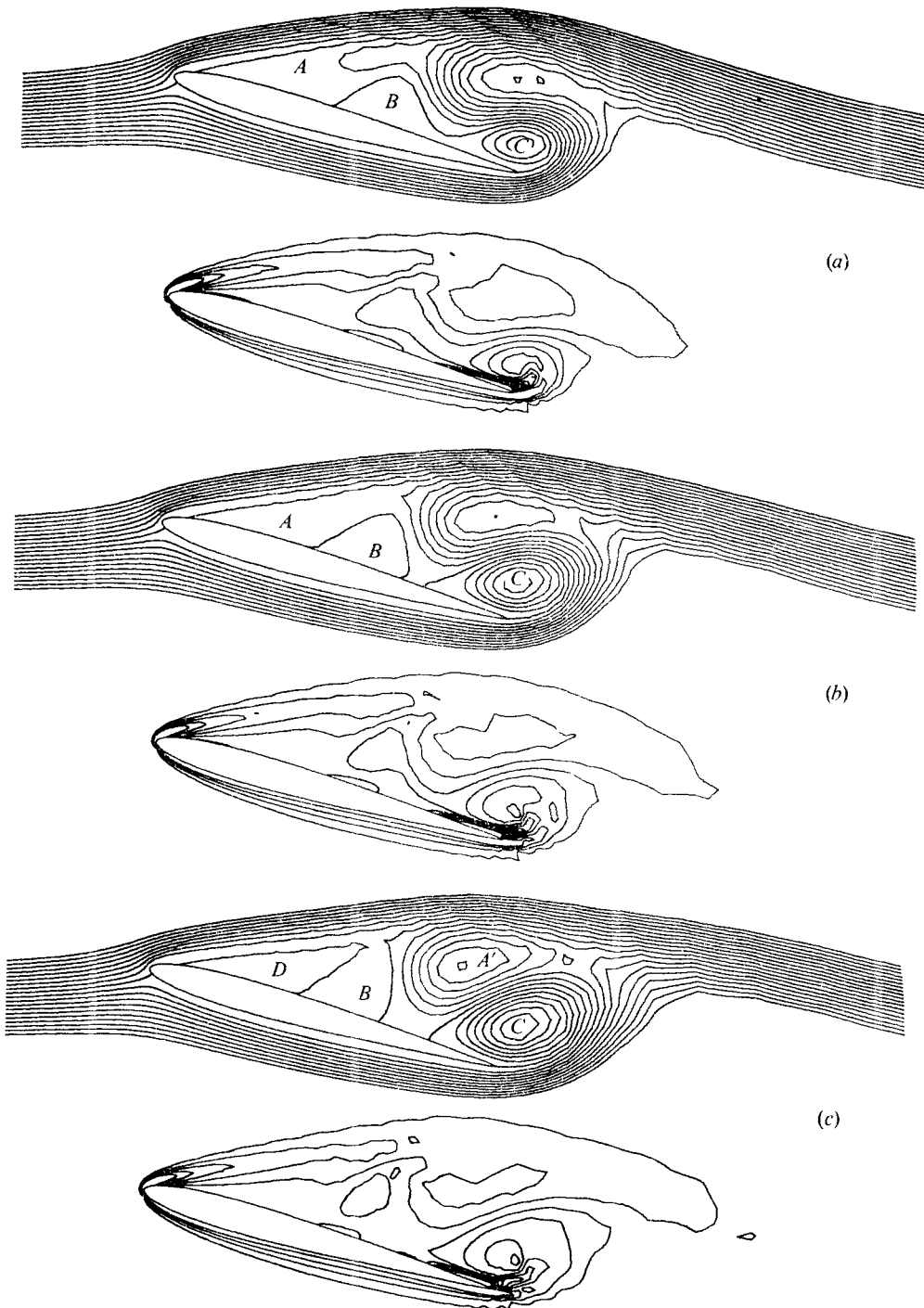


FIGURE 16. Streamlines and equi-vorticity lines. (a) $t = 16.212$.
(b) $t = 17.236$. (c) $t = 18.132$.

from the surface. Near the trailing edge, the movement of the separation point of bubble A' is helped by a small bubble observed at $t = 22.612$. (The reattachment and separation points are shown, respectively, in figures 12*b* and 4*f*.) The separation point of bubble A' and the reattachment point of this new bubble travel towards each other and merge (shown by the dashed line in figure 12*b*). Instantaneously, the separation point of bubble A' proceeds along the zero streamline (in the flow field) of this bubble to its separation point and makes it a part of bubble B . This phenomenon is similar to the one observed just after the impulsive start when the motion of the rear stagnation point towards the trailing edge is helped by a bubble. As the counterclockwise bubble C (which caused a loss in C_L) moves off the airfoil, the positive vorticity associated with it moves downstream and C_L increases (figure 11*c*). Hence, a second vortex is being shed near the trailing edge. After bubble A' bursts, the rate of increase of C_L with time falls and the further downstream motion of this bubble causes C_L to diminish. In other words, the gain in positive vorticity in the wake (downstream of the trailing edge) boosts C_L and the rise in negative vorticity lowers it. This is verified by a comparison of the equi-vorticity plots in figures 16*(c)* and 17*(a)* and *(b)* with figure 11*(c)*. Note that the process of bubble C moving off the surface does not result in the absence of the rear stagnation point as for bubble A (§6); thus, its leaving the surface is not categorized as bursting.

The trailing-edge pressure coefficient becomes less, relative to that at the front stagnation point, until bubble A' opens downstream. As for bubble A , it then rises. The bumps in the C_p distribution along the upper surface between $t = 18.772$ and 20.820 (figure 18*a*) correspond to bubble A' . The suction peak is low until after bubble C starts to leave the surface. The downstream motion of this bubble and its eventual lift-off from the surface intensify the suction peak. The clockwise bubble A' causes a decrease in pressure along the upper surface near the trailing edge and it counteracts the tendency of the counterclockwise bubble C to raise the pressure. Its influence is seen at $t = 20.820$ (figure 18*a*).

The front stagnation point moves up the airfoil during $t = 17.492$ –19.156 and then it moves down the surface, suggesting that circulation first decreases. This is substantiated by the variation of C_L in figure 11*(c)* and the motion of the dividing streamline. In addition, the development of counterclockwise bubbles B and C and the diminishing size and strength of bubble A' are suggested as the causes of the fall in C_L and C_D . Obviously then, the lift-off of bubble C must increase these loads; and after bubble A' ruptures, they diminish since it disengages itself from the surface. Just before bubble A' bursts, three bubbles are in contact with the surface, two clockwise bubbles and one counterclockwise bubble. Hence, C_L does not reach the previous high value (§6) when only one clockwise bubble is in contact with the surface.

The evolution of the flow field between $t = 23.380$ and 28.756 is shown by the instantaneous streamlines and equi-vorticity lines in figures 17*(c)* and 19. The strength of bubble B increases and subsequently the bubble disengages from the surface, producing a small bubble near the trailing edge; the separation point (or rear stagnation point) of the bubble remains near the trailing edge. In figure 17*(c)*, the point where the streamline $\Psi = 0.04$ crosses is a stagnation point.

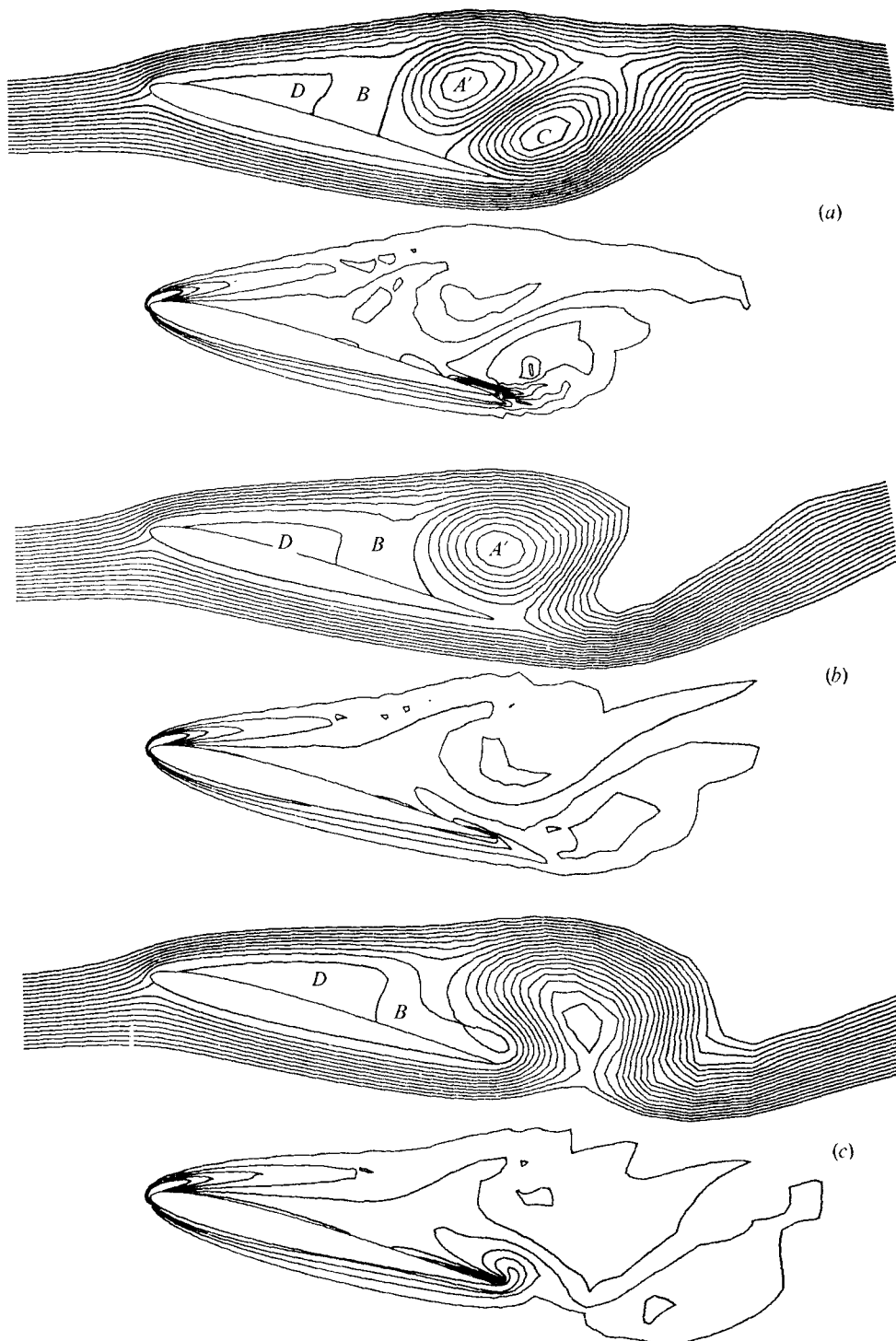


FIGURE 17. Streamlines and equi-vorticity lines. (a) $t = 19.284$.
(b) $t = 21.844$. (c) $t = 23.892$.

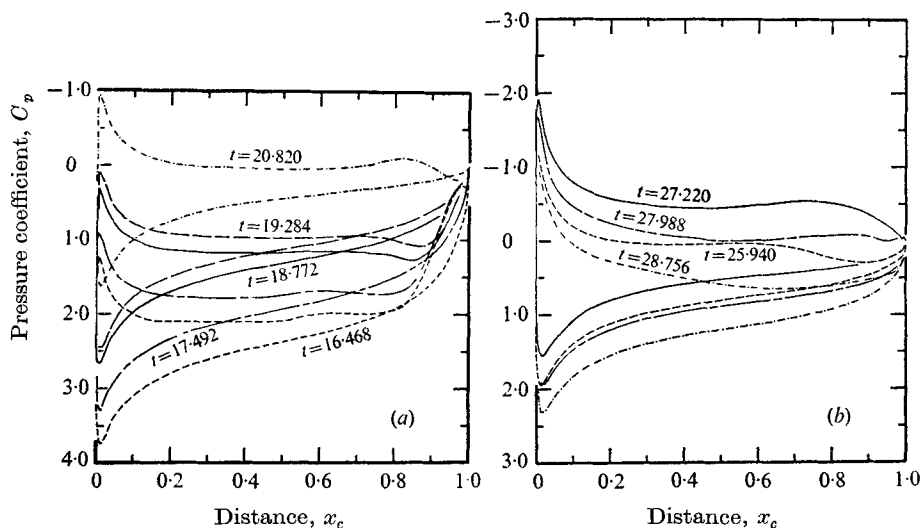


FIGURE 18. Surface pressure coefficients. $t = 16.468$ – 28.756 .

In an irrotational solenoidal flow such a crossing is at right angles (Batchelor 1967, pp. 105–106). In the presence of bubble B , the reattachment of bubble D , unlike that of bubble A , is normal to the surface and its centre is near the downstream end. In figure 19(b), a new bubble (E) is observed near the midsection of the airfoil. (Recall the formation of bubble B .) Furthermore, the reattachment of bubble D fails to occur. Unlike the bursting of bubble A and the subsequent development of bubble B , bubble E forms before bubble D ruptures. The separated streamline (bubble D) passes the trailing-edge region with the help of a very small bubble observed at $t = 27.220$ only. This phenomenon is the same as that reported when bubble A burst (§6). Bubble D is weaker than the original bubble A ; consequently, C_L is not as high as it is in the presence of bubble A (figure 11c). Figure 19(c) shows a new bubble (F) near the trailing edge (recall the formation of bubble C) and bubble E has moved downstream. A neck is produced downstream of the trailing edge in the $\omega = 1.0$ loop in figure 17(c); figure 19(a) shows that part of this loop is separated (cast off). As time advances, the region (downstream of the trailing edge) occupied by the positive vorticity extends and the negative vorticity is found in a smaller area. A vortex similar to the starting vortex is observed in figures 17(c) and 19(a) and (b). As this vortex grows, the lift rises (figure 11c). (The developments are similar to those relating to the shedding of bubble C .)

The surface C_p distributions are exhibited in figure 18(b). As indicated previously, when bubble A' bursts, its downstream displacement reduces the value of C_p at the trailing edge relative to its value at the front stagnation point. While bubble B is shed and bubble D extends, the above trend is reversed until bubble D bursts. The suction peak at $t = 27.220$ is less than that observed for bubble A under similar circumstances. The C_p distribution along the upper surface in contact with bubble D when $t = 25.940$ and 27.220 suggests the follow-

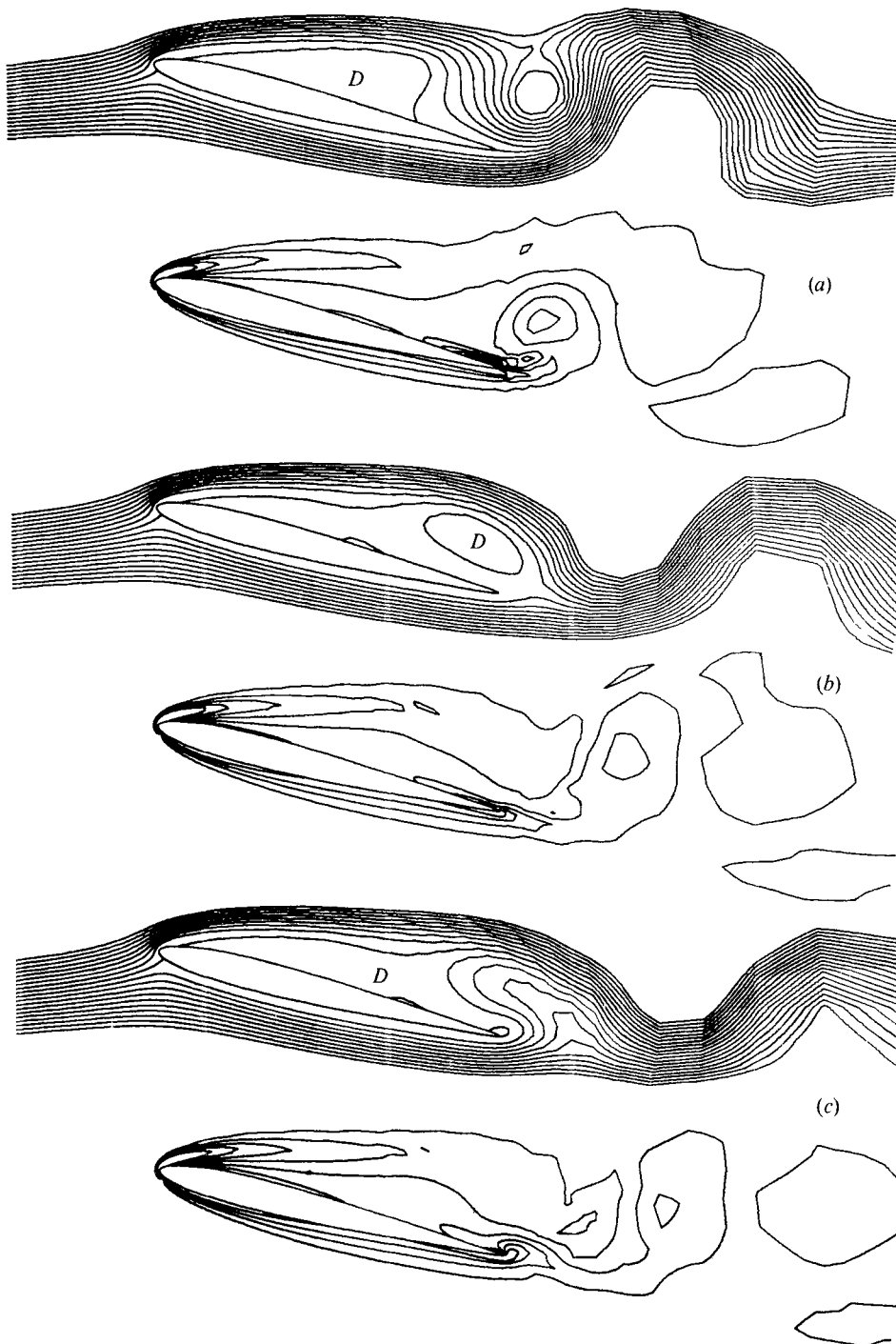


FIGURE 19. Streamlines and equi-vorticity lines. (a) $t = 25.684$,
(b) $t = 27.732$. (c) $t = 28.756$.

ing (as for bubble *A*). There are four distinct regions: (a) a region of positive pressure gradient just after the separation point, (b) a region of practically constant C_p , (c) a region of adverse pressure gradient that develops bubble *E*, and (d) a region of positive pressure gradient brought about by the tendency of bubble *D* to diminish the pressure. The bump in the C_p distribution corresponds to bubble *D*. Finally, when bubble *D* ruptures, a negative pressure gradient develops near the trailing edge and, subsequently, bubble *F* is formed.

The Strouhal number, defined as the ratio fd/U (where f is the shedding frequency and d a characteristic length scale), is 0.2162 with the chord as the characteristic length and 0.0589 on the basis of the projected height of the airfoil on the y axis. However, if d is taken as the width of the wake just downstream of the trailing edge defined by the maximum vertical distance between $\omega = 1.0$ and -1.0 at $t = 20.820$, then the Strouhal number is 0.1201. Obviously, these numbers will be different when the shedding frequency is established. It should be mentioned here that the factors governing the shedding frequency for bluff bodies are not completely understood. Several length parameters have been proposed for calculating the Strouhal number. Dikshit (1970) conducted experiments with a family of elliptical cylinders. He was unable to correlate results for very slender ellipses ($e = 0.92$ and 0.98) at small angles of attack ($\alpha < 20^\circ$).

Honji (1972) studied the nearly impulsive starting flow past a flat plate at $\alpha = 45^\circ$ and $R = 200$. Experiments were conducted in water with aluminium dust for flow visualization until shortly after bubbles *B* and *C* were formed. The flow development observed by Honji is similar to that reported in the numerical study by Lugt & Haussling (1972) for a 10% thick elliptical cylinder. There is a remarkable similarity between the streamline sequence Honji reported and that presented here even though α , R and the body shapes are different.

8. Concluding remarks

The unsteady flow around an airfoil has been solved through the use of finite-difference techniques. A versatile mathematical formulation is presented for investigating the flow past a flat plate, an elliptical cylinder or a Joukowski airfoil. Furthermore, any body that can be transformed into a circle (with no surface singularities) can be handled with only minor modifications. A new set of far boundary conditions is formulated. (Credit is due to Professor Morkovin for insisting on a proper set of conditions and for helping to formulate them.) The separation of the domain of calculation into rotational and irrotational parts allows a saving in computer costs. The development of a starting vortex and the production of circulation are explained. A distinction is made between a vortex and a bubble. The growth and intensification of separation bubbles and their role in influencing C_L are accounted for. The generation of unsteady lift and unsteady vortical formations have been studied. The stalling characteristics of a 9% thick, symmetric airfoil at an angle of attack of 15° with $R = 1000$ are sequentially traced. Numerical irregularities, reported by Lugt & Haussling (1972) for $R = 500$, are absent in the present study.

The main conclusions of this investigation are as follows. Immediately after

the impulsive start, both the front and rear stagnation points start moving. The rear stagnation point moves towards the trailing edge and the front stagnation point towards the leading edge. Within a very short time, the rear stagnation point arrives near the trailing edge with the help of a small bubble. The starting vortex has concentric equi-vorticity lines with a maximum in the centre. The value of C_L is large initially because of the impulsive start and it drops rapidly. The growth of circulation and change in its value are indicated by the movement of the front stagnation point and the dividing streamline upstream and downstream of the airfoil. The incipient separation (after the impulsive start) occurs downstream of the location where the magnitude of the vorticity is minimum (or where the gradient of vorticity along the surface is zero). Generally a bump in the pressure distribution along the upper surface of a smooth airfoil suggests the presence of a bubble. The downstream extension of a clockwise bubble causes it to burst, and the instantaneous streamlines from below the airfoil become part of this bubble, whereas a counterclockwise bubble opens to streamlines from above the airfoil as this bubble moves off the surface. The stalling characteristic of an airfoil is initiated when the clockwise bubble bursts. An increase in the strength of a clockwise (or a counterclockwise) bubble accompanies lower (or higher) pressures along the airfoil surface in contact with it. The lift increases when attached clockwise bubbles grow and when counterclockwise bubbles are swept away. It diminishes when counterclockwise bubbles grow and clockwise bubbles are shed. The rise or fall in the net positive vorticity in the wake increases or lowers the lift. Furthermore, the increase in net negative vorticity over the upper surface, with the vorticity in the wake practically the same, raises the lift.

Evidence provided by Honji (1972) and Lugt & Haussling (1972) suggests that all laminar flows around a stalled airfoil with leading-edge separation have the same basic topological character. Therefore, the specific lessons learned in this study on the behaviour of the time-dependent flow structure and force evolution are valid in general. This study may also be used as a stepping stone for investigating trailing-edge and dynamic stall of an oscillating airfoil or a stationary airfoil in an oscillating mean flow. Furthermore, it is hoped that this study of leading-edge stall will help in understanding stall conditions encountered in practice: (a) the separation bubble over a jet-flapped airfoil that fails to remain bottled up at the trailing edge and (b) the long laminar separation bubble that fails to reattach when undergoing transition to turbulence. These investigations require turbulence modelling and computers of the class of ILLIAC IV.

The authors express their gratitude to Professor Morkovin and Professor Fejer for frequent stimulating discussions and useful suggestions during the course of this work. Professor Morkovin has also constantly drawn our attention to the relevant references and provided valuable guidance. This research was supported under the Themis contract USAF F44620-69-C-0022 from the Air Force Office of Scientific Research. The final draft of this paper was prepared while the first author held an NRC-NASA Resident Research Associateship at the Ames Research Center.

REFERENCES

- ABBOTT, I. H. & VON DOENHOFF, A. F. 1959 *Theory of Wings Sections*. Dover.
- ARAKAWA, A. 1966 A computational design for the long term integration of the equations of atmospheric motion. *J. Comp. Phys.* **1**, 119.
- ARAKAWA, A. 1970 Numerical simulation of large-scale atmospheric motions. *SIAM-AMS Proc.* **2**, 24.
- BATCHELOR, G. K. 1967 *An Introduction to Fluid Dynamics*. Cambridge University Press.
- BROWN, S. N. & STEWARTSON, K. 1969 Laminar separation. *Ann. Rev. Fluid Mech.* **1**, 45.
- DIKSHIT, A. K. 1970 On the unsteady aerodynamics of stationary elliptic cylinders during organized wake condition. M.A. Sc. thesis, University of British Columbia.
- GOLDSTEIN, S. 1948 On laminar boundary-layer over a position of separation. *Quart. J. Mech. Appl. Math.* **1**, 43.
- HONJI, H. 1972 Starting flows past spheres and elliptic cylinders. *Rep. Res. Inst. Appl. Mech. Kyushu University*, vol. 19, no. 65.
- LUGT, H. J. & HAUSSLING, H. J. 1972 Laminar flows past elliptic cylinders at various angles of attack. *Naval Ship R. & D. Center Rep.* no. 3748.
- MEHTA, U. B. 1972 Starting vortex, separation bubbles, and stall – a numerical study of laminar unsteady flow around an airfoil. Ph.D. thesis, Illinois Institute of Technology.
- PRANDTL, L. 1952 *Essentials of Fluid Dynamics*. Hafner.
- PRANDTL, L. & TIETJENS, O. G. 1934 *Applied Hydro- and Aeromechanics*. McGraw-Hill.
- SEARS, W. R. & TELIONIS, D. P. 1971 Unsteady boundary-layer separation. In *Recent Research of Unsteady Boundary Layers, Proc. Int. Un. Theor. Appl. Mech., Quebec*, vol. 1 (ed. E. A. Eichelbrenner), pp. 404–447.
- STUART, J. T. 1971 Unsteady boundary layers. In *Recent Research of Unsteady Boundary Layers, Proc. Int. Un. Theor. Appl. Mech., Quebec*, vol. 1 (ed. E. A. Eichelbrenner), p. 28.
- TANEDA, S. 1972 The development of the lift of an impulsively started elliptic cylinder at incidence. *J. Phys. Soc. Japan*, **33**, 1706.
- THWAITES, B. 1960 *Incompressible Aerodynamics*. Oxford University Press.
- WANG, C.-Y. 1971 Comments 'on Unsteady Boundary Layers. W. R. Sears & D. R. Telionis. In *Recent Research of Unsteady Boundary Layers, Proc. Int. Un. Theor. Appl. Mech., Quebec*, vol. 1 (ed. E. A. Eichelbrenner), p. 442.
- WOODS, L. C. 1954 A note on the numerical solution of fourth-order differential equations. *Aero. Quart.* **5**, 176.